RSC Advances

PAPER

View Article Online
View Journal | View Issue

Cite this: *RSC Adv.*, 2021, **11**, 32707

Luminescence and energy transfer of warm white-emitting phosphor $Mg_2Y_2Al_2Si_2O_{12}:Dy^{3+},Eu^{3+}$ for white LEDs

Zizhong Zhu,[a] Chunjing Tao,[b] Zhijun Wang,[b] Zhiping Yang[b] and Panlai Li *[b]

A series of $Mg_2Y_2Al_2Si_2O_{12}:Dy^{3+},Eu^{3+}$ phosphors were synthesized by the solid-state method. The luminescent properties and crystal structures of the $Mg_2Y_2Al_2Si_2O_{12}:Dy^{3+},Eu^{3+}$ phosphors were analyzed. The XRD results show that the synthesized $Mg_2Y_2Al_2Si_2O_{12}:Dy^{3+},Eu^{3+}$ phosphors are of pure phase. $Mg_2Y_2Al_2Si_2O_{12}:Dy^{3+}$ can emit blue and yellow light under 367 nm light excitation; when doped with Eu^{3+}, there is an obvious energy transfer from Dy^{3+} to Eu^{3+}, and warm white light can be realized by adjusting the concentrations of Dy^{3+} and Eu^{3+} in $Mg_2Y_2Al_2Si_2O_{12}$. A warm white LED device was fabricated by combining $Mg_2Y_{1.88}Al_2Si_2O_{12}:0.05Dy^{3+},0.07Eu^{3+}$ and a UV LED chip (370 nm) under a voltage of 3.2 V and current of 5 mA, the characteristics of the white LED being CIE = (0.4071, 0.3944), CCT = 3500 K and CRI = 91.3.

Received 17th August 2021
Accepted 18th September 2021

DOI: 10.1039/d1ra06215h

rsc.li/rsc-advances

1. Introduction

The blue light may be inevitably harmful to the human body, and long-term use is not conducive to health. Therefore, a white light-emitting diode (LED) is obtained by exciting single matrix fluorescent powder with ultraviolet (UV) or near-UV light, and UV light will not affect white light.[1–5] Dy^{3+} ions have blue emission peaks (480 nm, $^4F_{9/2} \rightarrow {}^6H_{15/2}$) and yellow emission peaks (575 nm, $^4F_{9/2} \rightarrow {}^6H_{13/2}$). White light can be realized by coordinating the ratio of blue light and yellow light.[6–11] Sehrawat *et al.* prepared cold white light-emitting perovskite $SrLa_2A1_2O_7:Dy^{3+}$ nanophosphors.[10] Xu *et al.*[11] studied the luminescent properties of $Sr_4Ca(PO_4)_2SiO_4:Dy^{3+}$. When the doping concentration of Dy^{3+} ion is equal to 0.04, the phosphor emits cold white light, and the luminescent intensity increases by 1.7 times when the charge compensation Li^+ ion is added. Zhang *et al.*[12] prepared $Ca_8ZnY(PO_4)_7:Dy^{3+}$; the photoluminescence of $Ca_8ZnY(PO_4)_7:0.12Dy^{3+}$ was enhanced by adding Mg^{2+} and B^{3+}, and the thermal stability was improved after introducing Mg^{2+}. However, generally, a Dy^{3+} ion single-doped fluorescent material emits cold white light with low index, and hence red light needs to be added to improve the index. Up to now, Eu^{2+}, Mn^{2+}, Eu^{3+} and Mn^{4+} have been the most common red emission activators, but the emission spectra of Eu^{2+} and Mn^{2+} may extend to the deep red band, making it difficult to maintain high color purity.[13–17] Eu^{3+}- and Mn^{4+}-doped red phosphors have attracted extensive attention due to their narrow line emission and good color purity. Mn^{4+} has two broad excitation bands in the UV (300–400 nm) and blue (400–500 nm) regions. When a white LED is synthesized by Mn^{4+}-activated red fluorescent powder and blue and green fluorescent powder, the excitation band in the blue region causes strong reabsorption and the output of white light will be affected.[17,18] Eu^{3+} can emit orange and red light, which is required by most lighting and display applications.[19–22] Leow *et al.*[21] synthesized a series of Eu^{3+} and Dy^{3+} co-doped $BaB_2Si_2O_8$ by the solid-state method, realizing adjustable emission of white light to red light. Hussain *et al.*[22] prepared $K_3La(VO_4)_2:Dy^{3+}/Eu^{3+}$ by the sol–gel method, and warm white light was observed as a result of an effective energy transfer.

The garnet structure has high structural stability and has potential application value for the research and development of the luminescence properties of fluorescent materials.[23–26] Pan

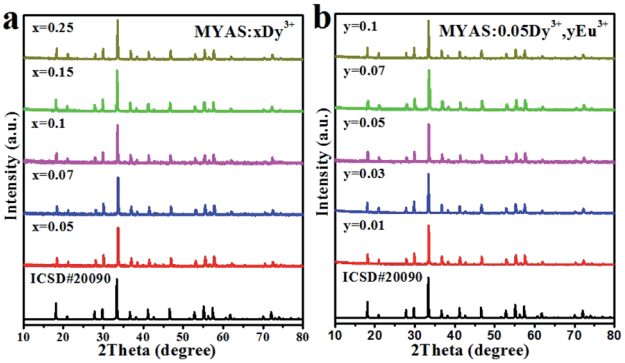

Fig. 1 XRD patterns of $Y_3Al_5O_{12}$ (ICSD#20090) standard card and (a) MYAS:xDy^{3+} and (b) MYAS:Dy^{3+},yEu^{3+}.

[a]*College of Physics Science & Technology, Tangshan Normal University, Tangshan 063000, China*

[b]*College of Physics Science & Technology, Hebei University, Baoding 071002, China. E-mail: li_panlai@126.com*

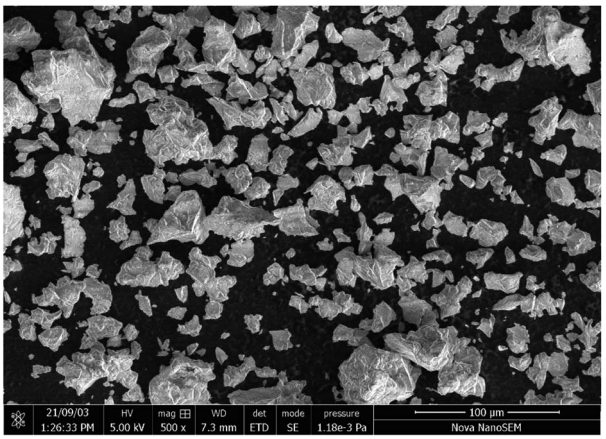

Fig. 2 SEM image of MYAS:0.05Dy^{3+}.

et al.[26] obtained white light by doping Ce^{3+} in an $Mg_2Y_2Al_2Si_2O_{12}$ matrix and exciting it with a blue LED. Tang combined $Lu_3Mg_2GaSi_2O_{12}$:0.015Ce and 0.03Sm samples with commercially available red phosphors and blue chips to obtain a warm white LED with a color rendering index of 86.6 and a color temperature of 3592 K.[25] Wei integrated a 450 nm LED chip with a $Y_{1.95}Ce_{0.05}Mg_2Al_2Si_2O_{12}$ phosphor.[27] The completed LED device emitted white light, with a CCT value of 4363 K and a CRI value of 83.7. Zhang reported $Y_2Mg_2Al_2Si_2O_{12}$:Ce^{3+},Mn^{2+} phosphors for warm-color white LEDs, which are suitable for the current mainstream blue LED chips.[28] Therefore, in this work, a Dy^{3+} and Eu^{3+} co-doped $Mg_2Y_2Al_2Si_2O_{12}$ (MYAS) phosphor was prepared, and its luminescent properties were studied in detail. By accurately adjusting the doping concentration and proportion of Dy^{3+} and Eu^{3+}, we have achieved high-quality warm white-light emission from a single substrate.

Table 1 Radius difference between Dy^{3+} ion and cation in matrix

R_m	R_d	D_r
Mg1 (0.89 Å, $N = 8$)	Dy (1.027 Å, $N = 8$)	14.3%
Y1 (1.019 Å, $N = 8$)	Dy (1.027 Å, $N = 8$)	0.8%
Mg2 (0.72 Å, $N = 6$)	Dy (0.912 Å, $N = 6$)	21.1%
Al1 (0.535 Å, $N = 6$)	Dy (0.912 Å, $N = 8$)	41.3%

2. Experimental section

2.1 Materials and synthesis

MYAS:Dy^{3+}/Eu^{3+} was synthesized by the high-temperature solid-state method. The raw materials were MgO (99.9%), Y_2O_3 (99.9%), Al_2O_3 (99.9%), SiO_2 (99.9%), Dy_2O_3 (99.9%) and Eu_2O_3 (99.9%). The precursors were thoroughly mixed and ground. Then, the mixed materials were transferred to a crucible and placed in a sintering furnace for synthesis reaction at 1500 °C for 3 hours. Finally, the sample was cooled to room temperature and ground completely.

2.2 Materials characterization

The crystal structure of the samples was characterized using a D8-A25 focusing diffractometer. A structural analysis system (GSAS) was used to analyze the structure. Photoluminescence and photoluminescence excitation spectra were measured with a Hitachi F4600. The decay curve was obtained using a HORIBA FL-1057 device with a xenon lamp as excitation source. Color coordinates were measured with a PMS-80 color analyzer obtained commercially at room temperature.

3. Results and discussion

3.1 XRD patterns of $Mg_2Y_2Al_2Si_2O_{12}$:xDy^{3+},yEu^{3+}

Fig. 1(a) and (b) show the XRD results of MYAS:xDy^{3+} and MYAS:Dy^{3+},yEu^{3+}. The diffraction peaks of all samples are

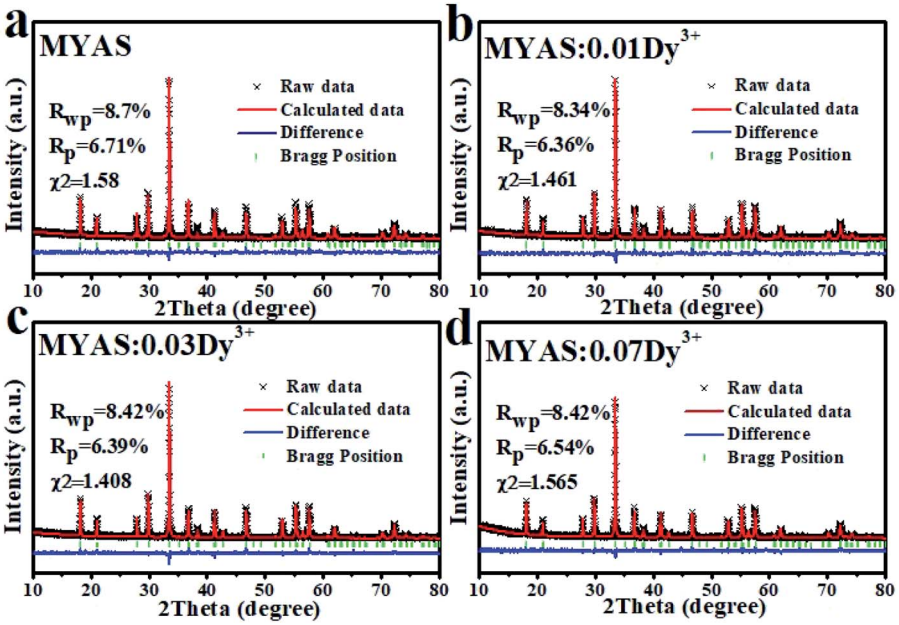

Fig. 3 Refinement result of MYAS:xDy^{3+}: (a) $x = 0$, (b) $x = 0.01$, (c) $x = 0.03$, (d) $x = 0.07$.

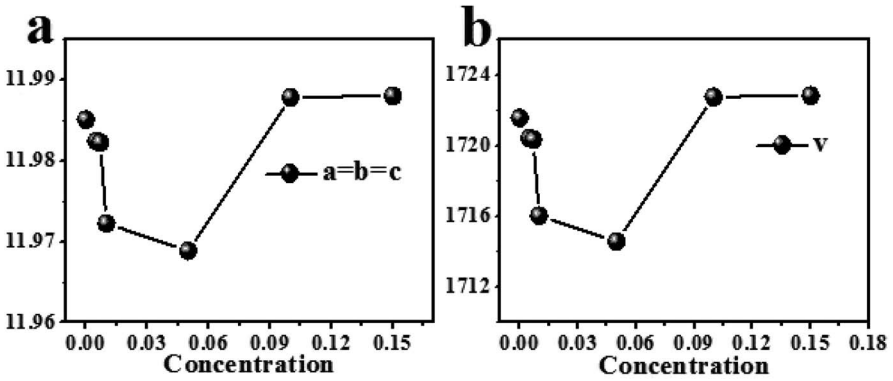

Fig. 4 (a) Cell parameters and (b) cell volume changes of MYAS:xDy^{3+}.

consistent with the structure of the standard card $Y_3Al_5O_{12}$ (ICSD#20090) and there are no other miscellaneous peaks,[25] which indicate that the synthesized MYAS:xDy^{3+} and MYAS:x-Dy^{3+},yEu^{3+} have garnet structure. Also, the diffraction peaks have no obvious shift, which indicates that the lattice distortion caused by Dy^{3+} replacing Y^{3+} is very small, and therefore it is proved that all the synthesized samples are in a single crystal phase.

Fig. 2 shows an SEM image of MYAS:0.05Dy^{3+},Eu^{3+}. It can be seen that the phosphor is composed of irregular particles with a particle size of 5–20 μm.

Analysis was conducted in order to further understand the influence of Dy^{3+} on the lattice parameters of MYAS after entering the lattice of the matrix. According to the standard card ICSD#20090, MYAS:xDy^{3+} (x = 0, 0.01, 0.03, 0.07, 0.1, 0.15) is refined with GASA software, and the final result is shown in Fig. 3. From Fig. 3(a)–(d), it can be seen that the experimental data (red line) and the calculated data (black line) are very consistent. It can be seen that the χ^2, R_p and R_{wp} obtained by refinement are all within the experimental range (χ^2 < 10%, R_p and R_{wp} < 15%), proving that Dy^{3+} has successfully entered the matrix and is a pure phase. In the doping process, the radius difference between doped ions and substituted ions should be within 30%, as shown in eqn (1):[29–31]

$$D_r = 100 \times \left| \frac{R_m(N) - R_d(N)}{R_m(N)} \right| \quad (1)$$

The radius difference calculated by eqn (1) is shown in Table 1. From the results, it can be seen that the differences in ionic radii of the eight-coordinated Mg1, Y and the six-coordinated Mg2 are all less than 30%, so Dy^{3+} may replace the eight-coordinated Mg1 and the six-coordinated Mg2.

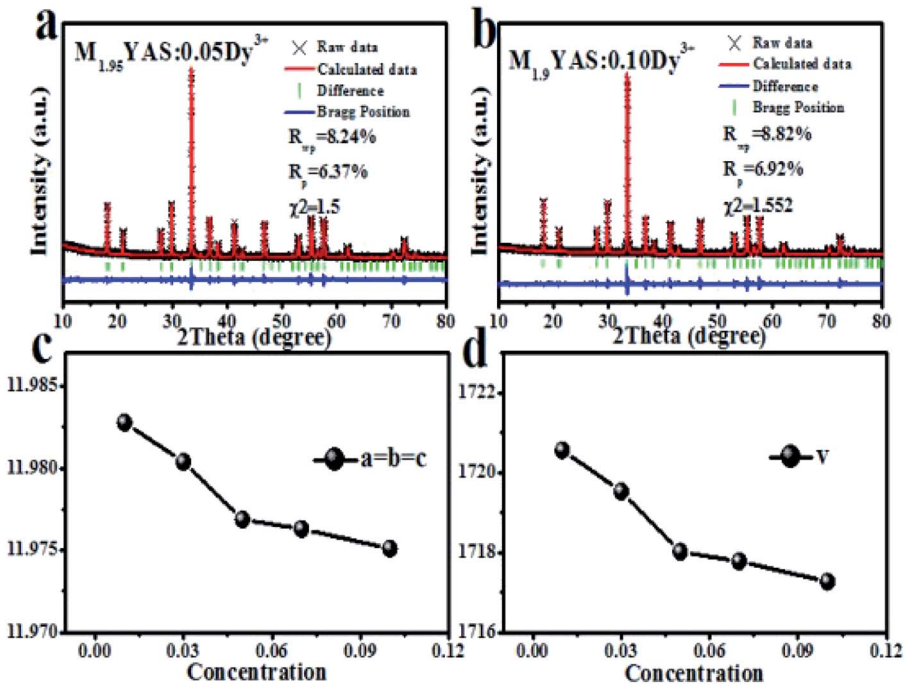

Fig. 5 Refinement results of M_{2-x}YAS:xDy^{3+}: (a) x = 0.05, (b) x = 0.1. (c) Cell parameters and (d) cell volume of M_{2-x}YAS:xDy^{3+}.

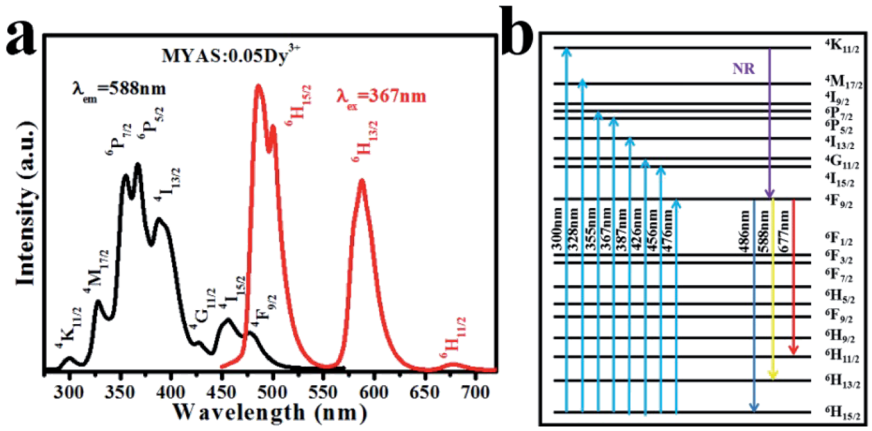

Fig. 6 (a) Excitation spectrum and emission spectrum of MYAS:xDy^{3+} and (b) Dy^{3+} energy level diagram.

Because the radius (r = 1.03, CN = 8) of Dy^{3+} is larger than the radius[30] of Y^{3+} (r = 1.02, CN = 8), when Y^{3+}is replaced by Dy^{3+}, the cell parameter and cell volume will both become larger, but it can be seen from Fig. 4(a) and (b) that the cell parameter and cell volume first decrease and then increase with increasing Dy^{3+} concentration. This is because Mg^{2+} and Y^{3+} occupy the same lattice position in the MYAS crystal; hence the decrease in cell parameter and cell volume of MYAS:xDy^{3+} is caused by the partial substitution of Dy^{3+} for Mg^{2+}(r = 0.89, CN = 8) in the same lattice position.

In order to further determine the cell parameters and the reasons for the reduction of cell volume, Fig. 5 shows the refined results. The cell parameters and cell volume decrease with an increase of Dy^{3+} doping concentration. When Dy^{3+} is used to replace Mg^{2+} ions in the same lattice position, the charge is unbalanced, thus generating cation vacancies, as shown in eqn (2), and the generation of cation vacancies is helpful to the contraction of the unit cell:[29]

$$2Dy^{3+} = 2Mg^{2+} + VMg^{2+} \quad (2)$$

3.2 Luminescence characteristics of $Mg_2Y_2Al_2Si_2O_{12}$:xDy^{3+}

Fig. 6(a) shows the excitation spectrum and emission spectrum of MYAS:0.05Dy^{3+}. For 588 nm emission, the excitation can

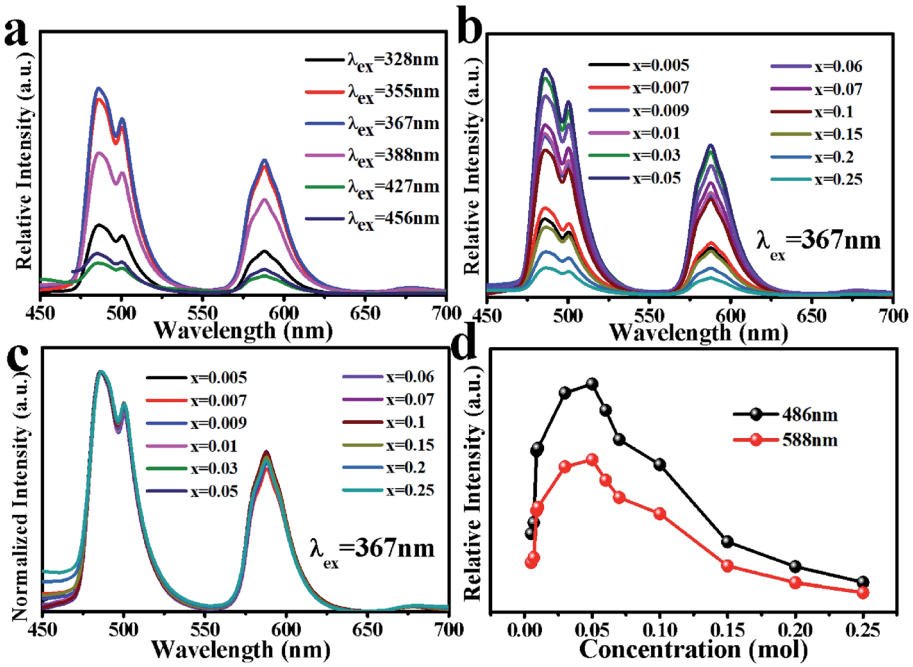

Fig. 7 (a) Emission spectrum of MYAS:0.05Dy^{3+} under different excitation wavelengths. (b) Emission spectrum of MYAS:xDy^{3+} (x = 0–0.25) under 367 nm excitation. (c) Normalized emission spectrum of MYAS:xDy^{3+} (x = 0–0.25) under 367 nm excitation. (d) Variation of emission intensity of MYAS:xDy^{3+}.

Table 2 Y/B ratio of MYAS:xDy^{3+}

Concentration	Y/B	Concentration	Y/B
0.005	0.61	0.06	0.66
0.007	0.63	0.07	0.66
0.009	0.63	0.10	0.66
0.01	0.64	0.15	0.65
0.03	0.66	0.20	0.65
0.05	0.67	0.25	0.65

range from 250 to 500 nm, and the maximum peak is at 367 nm, which mainly comes from the $^6H_{15/2} \rightarrow {}^6P_{5/2}$ transition of Dy^{3+},[31–34] and the excitation spectrum of Dy^{3+} covers almost all areas from UV light to blue light. In the emission spectrum, due to the transition of $^4F_{9/2} \rightarrow {}^6H_{J/2}$ (J = 11, 13, 15) of Dy^{3+}, three emission peaks at about 486, 588 and 677 nm were obtained respectively, and the two main emission peaks were located in the blue (486 nm) and yellow (588 nm) regions.[21] In general, the luminous intensity of $^4F_{9/2} \rightarrow {}^6H_{15/2}$ of Dy^{3+} is higher than that of $^4F_{9/2} \rightarrow {}^6H_{13/2}$, indicating that Dy^{3+} occupies an inverted symmetry center lattice position in the matrix.[22] The intensity of the 486 nm emission is higher than that of 588 nm, as shown in Fig. 6(a), which indicates that Dy^{3+} occupies the lattice position of the inversion symmetry center in the MYAS matrix. The energy level diagram of Dy^{3+} is shown in Fig. 6(b).

Fig. 7 shows the luminescence intensity of Dy^{3+} with various doping concentrations of Dy^{3+} under 367 nm excitation (x = 0.005, 0.007, 0.009, 0.01, 0.03, 0.05, 0.06, 0.07, 0.1, 0.15, 0.2, 0.25). The emission intensity of Dy^{3+} increases continuously at 486 nm and 588 nm. When x = 0.05, the intensity reaches the maximum, and then as the concentration of Dy^{3+} continues to increase, the intensity decreases at 486 nm and 588 nm.

In order to study the influence of Dy^{3+} doping concentration on the luminescent color of MYAS:xDy^{3+}, the relative intensity ratio of yellow (588 nm) and blue (486 nm) regions under 367 nm UV excitation was determined. As shown in Table 2, it can be seen that with the increase of Dy^{3+} doping concentration, the Y/B ratio increases first.

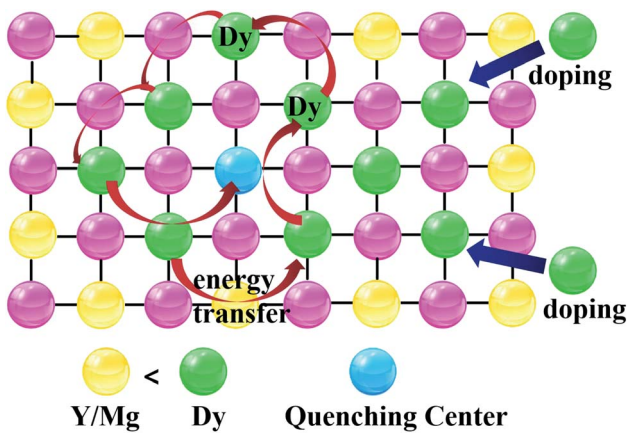

Fig. 8 Schematic diagram of concentration quenching process of Dy^{3+}.

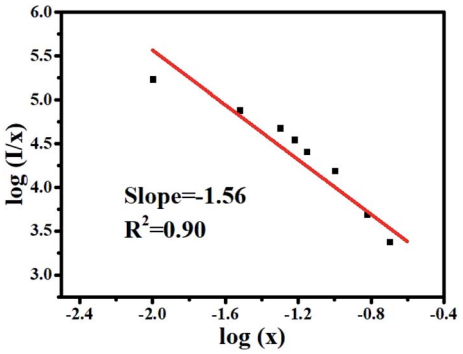

Fig. 9 Graph of log(I/x) and log(x) for MYAS:xDy^{3+}.

The reason why the emission intensity of Dy^{3+} increases first and then decreases is that concentration quenching occurs between Dy^{3+}, which involves the energy transfer of activator ions at high concentration.[35–38] Fig. 8 explains the concentration quenching of Dy^{3+}. As the doping concentration of Dy^{3+} ions increases, the distance between ions decreases continuously, and the exchange interaction between Dy^{3+} ions is strengthened. When the center distance between Dy^{3+} ions is less than the critical distance, the tunneling effect is easy to occur, resulting in cascade energy transfer, resulting in luminescence quenching.[38,39]

In order to further explore the concentration quenching mechanism of Dy^{3+}, one can consider the Blasse formula:[38–40]

$$R_c = 2[3V/4\pi X_c N]^{1/3} \quad (3)$$

For the MYAS matrix, the value of V is 1721.583, $N = z = 6$, X_c = 5%, and calculated R_c = 22.21, which is far greater than 5. Therefore, the concentration quenching mechanism of Dy^{3+} involves a multipolar interaction.

According to the theories of Dexter and Van Uitert, the luminous intensity I of Dy^{3+} ions follows the following formula:[37–40]

$$\frac{I}{x} = K\left[1 + \beta(x)^{\frac{\theta}{3}}\right]^{-1} \quad (4)$$

As shown in Fig. 9, θ is 4.68, which is close to 6, indicating that the concentration quenching mechanism of Dy^{3+} in the MYAS matrix involves dipole–dipole interaction.

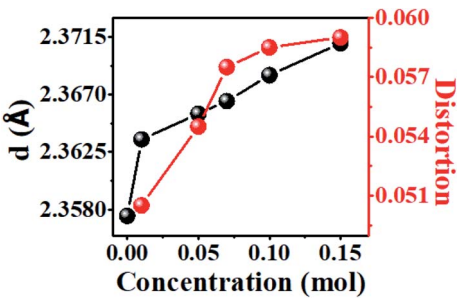

Fig. 10 MYAS:xDy^{3+}: changes in bond length and twist of Y/Mg(1)O$_8$.

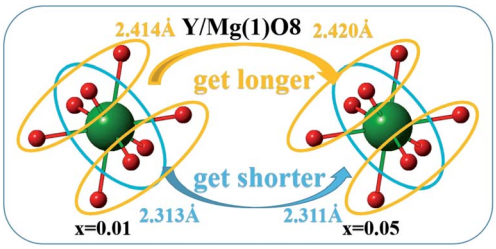

Fig. 11 MYAS:xDy^{3+} (x = 0.01, 0.05): Y/Mg(1)O_8 bond length change.

The increase of Y/B ratio is due to the change of dodecahedron symmetry. The yellow emission of Dy^{3+} results from supersensitive transition and is related to local symmetry. With an increase of Dy^{3+} doping concentration, the average bond length of dodecahedron Y/Mg(1)O_8 gradually becomes longer because the radius of Dy^{3+} is larger than that of Y^{3+} (r = 1.02) (Fig. 10). The bond length between the luminescent center and the surrounding ligand changes, and the twist degree of the polyhedron in which it is located also changes. The twist degree of the crystal can be calculated by formula (5):[38,39]

$$D(\mathrm{TO}) = \left(\sum_{i=1}^{8} \mathrm{TO}_i - \mathrm{TO}_m\right) \Big/ 8\mathrm{TO}_m \quad (5)$$

Fig. 10 shows the twist degree of crystal Y/Mg(1)O_8. As the doping concentration of Dy^{3+} increases, the twist degree of the crystal gradually increases, causing the yellow light in the emission spectrum of Dy^{3+} to increase, resulting in an increase in the Y/B ratio.

Fig. 11 depicts the reason why the symmetry of dodecahedron Y/Mg(1)O_8 decreases. By comparing the bond lengths of dodecahedron Y/Mg(1)O_8, it is found that the shorter bond lengths are getting shorter and the longer bond lengths are getting longer, which leads to the reduction of symmetry of dodecahedron Y/Mg(1)O_8. The symmetry of dodecahedron Y/Mg(1)O_8 decreases, indicating that the proportion of yellow light is gradually increasing (Table 2).

3.3 Luminescence properties of $Mg_2Y_{1.95}Al_2Si_2O_{12}$:0.05Dy^{3+},$y$Eu^{3+}

Fig. 12(a) shows the emission spectrum of MYAS:0.05Dy^{3+} and the excitation spectrum of MYAS:0.05Dy^{3+},0.05Eu^{3+}. It can be seen that the emission spectrum of Dy^{3+} and the excitation spectrum of Eu^{3+} obviously overlap, which indicates that there may be energy transfer from Dy^{3+} to Eu^{3+}. Fig. 12(b) shows the emission spectrum of MYAS:0.05Dy^{3+},yEu^{3+} (y = 0–0.1) excited at 367 nm. The emission spectrum includes not only blue and yellow emission of Dy^{3+} ($^4F_{9/2} \rightarrow {}^6H_{15/2}$ and $^4F_{9/2} \rightarrow {}^6H_{13/2}$), but also characteristic emission of Eu^{3+} ($^5D_0 \rightarrow {}^7F_J$ (J = 2, 3, 4)). The emission peaks at 611 nm, 633 nm and 714 nm correspond to the $^5D_0 \rightarrow {}^7F_2$, $^5D_0 \rightarrow {}^7F_3$ and $^5D_0 \rightarrow {}^7F_4$ electron transitions of Eu^{3+}, respectively.[22,24] From the normalized emission spectrum, it can be clearly seen that the proportion of yellow light is increasing significantly (Fig. 12(c)). As the concentration of doped Eu^{3+} ions increases, the emission intensity at 486 nm and 588 nm (Dy^{3+}) decreases, and the emission intensity of Eu^{3+} (611

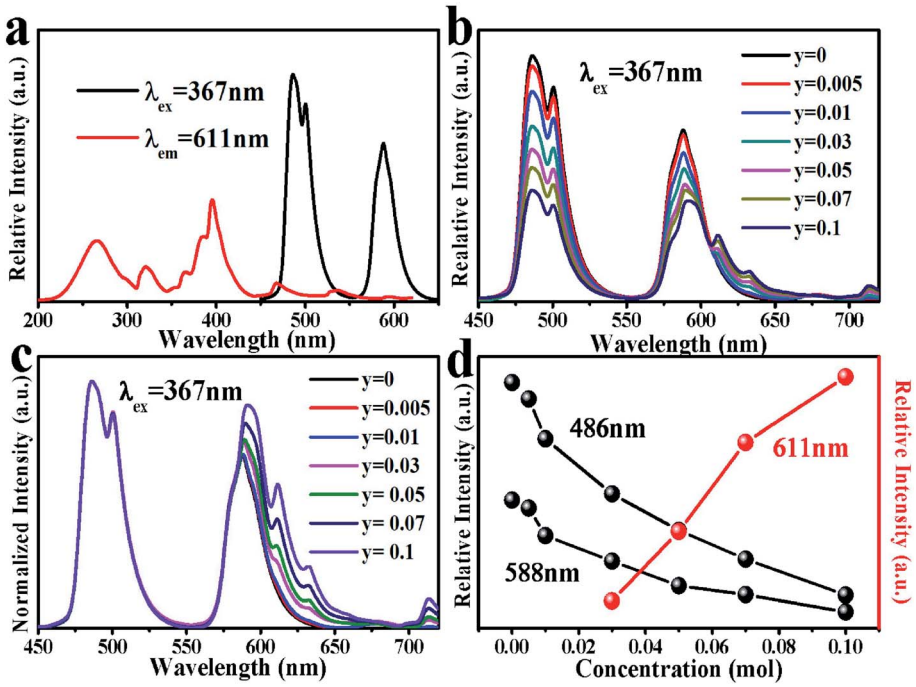

Fig. 12 (a) Emission spectrum of MYAS:0.05Dy^{3+} and excitation spectrum of MYAS:0.05Dy^{3+},0.05Eu^{3+}. (b) Emission spectrum of MYAS:0.05-Dy^{3+},yEu^{3+} (y = 0–0.1) under 367 nm excitation. (c) Normalized emission spectrum of MYAS:xDy^{3+},yEu^{3+} under 367 nm excitation. (d) Variation of emission intensity of MYAS:xDy^{3+},yEu^{3+}.

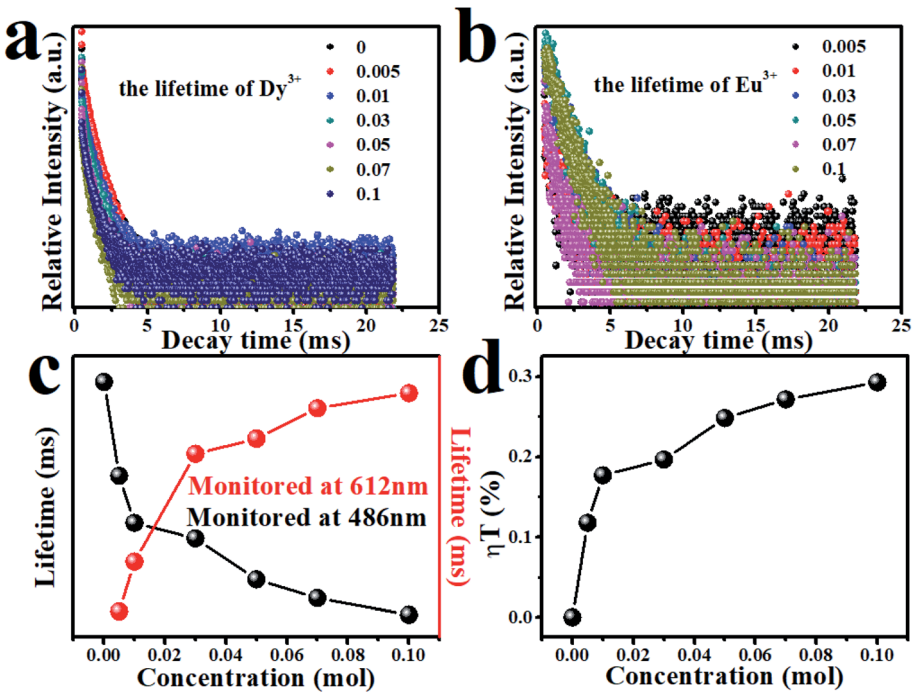

Fig. 13 Fluorescence attenuation curves of MYAS:0.05Dy^{3+},yEu^{3+} ($y = 0$–0.1): (a) detection at 486 nm (Dy^{3+}); (b) detection at 612 nm (Eu^{3+}). (c) Calculated MYAS:0.05Dy^{3+},yEu^{3+} ($y = 0$–0.1) lifetime. (d) Energy transfer efficiency from Dy^{3+} to Eu^{3+}.

nm) increases (Fig. 12(d)). The emission intensity of Dy^{3+} decreases continuously, and the reason why the emission intensity of Eu^{3+} increases continuously may be that Dy^{3+} transfers more and more energy to Eu^{3+}, which proves that energy transfer from Dy^{3+} to Eu^{3+} does occur.

That there is energy transfer between Dy^{3+} ions and Eu^{3+} ions can be verified by Fig. 13(a) and (b).

Dy^{3+} and Eu^{3+} lifetimes τ can be calculated by formula (6):[24,25,28]

$$\tau^* = A_1\tau_1^2 + A_2\tau_2^2/A_1\tau_1 + A_2\tau_2 \quad (6)$$

The lifetimes of Dy^{3+} and Eu^{3+} calculated by formula (6) are shown in Fig. 13(c) in the form of a line chart. With an increasing doping concentration of Eu^{3+}, the lifetimes of Dy^{3+} become shorter and shorter (1.84, 1.62, 1.51, 1.47, 1.38, 1.34, 1.30 ms), which verifies that there is indeed energy transfer between Dy^{3+} and Eu^{3+} ions.

The energy transfer efficiency between Dy^{3+} and Eu^{3+} can be calculated by formula (7):[39]

$$\eta_T = 1 - \tau_s/\tau_{s0} \quad (7)$$

Fig. 13(d) shows the energy transfer efficiency between Dy^{3+} and Eu^{3+}. The energy transfer efficiency between Dy^{3+} and Eu^{3+}gradually increases with an increase of Dy^{3+} ion concentration in the MYAS matrix. When $y = 0.10$, the energy transfer efficiency can reach 30%.

In order to determine the type of interaction between Dy^{3+} and Eu^{3+}, the critical distance between Dy^{3+} and Eu^{3+} can be obtained from eqn (3). The calculated value of the critical distance R_c between Dy^{3+} and Eu^{3+} is greater than 5, so the

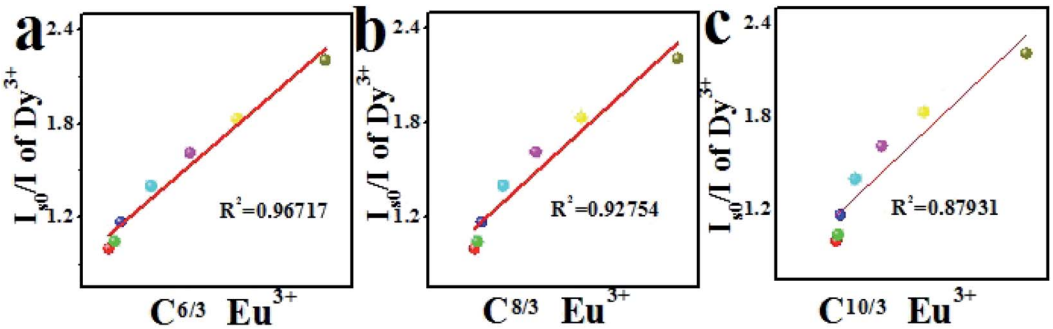

Fig. 14 Diagram of I_{s0}/I and $C^{\alpha/3}$ of MYAS:0.07Dy^{3+},yEu^{3+} for (a) $\alpha = 6$, (b) $\alpha = 8$, (c) $\alpha = 10$.

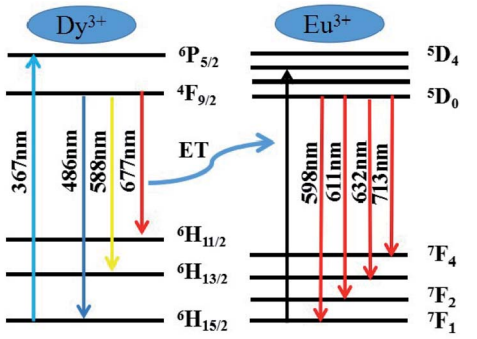

Fig. 15 Energy transfer mechanism diagram of MYAS:0.05Dy^{3+},yEu^{3+}.

energy transfer mechanism between Dy^{3+} and Eu^{3+} involves a multilevel interaction.

To further determine the energy transfer mechanism between Dy^{3+} and Eu^{3+}, the following formula can be used for calculation:[40]

$$\eta_{s0}/\eta = C^{\alpha/3} \quad (8)$$

Since quantum efficiency is difficult to obtain, formula (9) can be used instead:[39,40]

$$(I_{s0}/I) = C^{\alpha/3} \quad (9)$$

As can be seen from Fig. 14(a)–(c), for MYAS:0.05Dy^{3+},yEu^{3+}, when $\alpha = 6$, a best fitting line can be obtained, and R^2 for this case is 0.96717. Therefore, the energy transfer mechanism of $Dy^{3+} \rightarrow Eu^{3+}$ involves dipole–dipole interaction.

In order to further understand the mechanism of energy transfer between Dy^{3+} and Eu^{3+}, Fig. 15 shows the mechanism diagram of energy transfer. For MYAS:Dy^{3+},Eu^{3+}, there is overlap between the emission spectrum of Dy^{3+} and the excitation spectrum of Eu^{3+}. Part of the emission of Dy^{3+} will be reabsorbed by Eu^{3+}, resulting in $^5D_0 \rightarrow {}^7F_J$ (J = 1, 2, 3, 4) electron transition of Eu^{3+}.

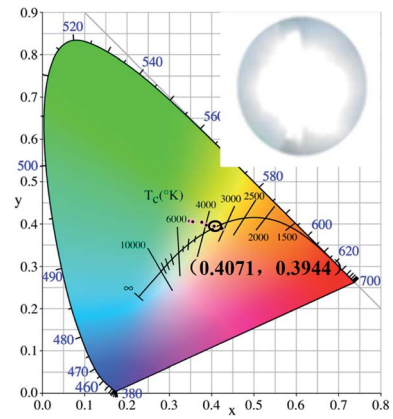

Fig. 16 Color coordinates of MYAS:0.05Dy^{3+},yEu^{3+} (y = 0–0.1), and the warm white LED device (MYAS:0.05Dy^{3+},0.07Eu^{3+} + 370 nm UV LED chip) under a voltage of 3.2 V and current of 5 mA (CIE = (0.4071, 0.3944), CCT = 3500 K, CRI = 91.3).

Table 3 Color coordinate values of MYAS:xDy^{3+} and MYAS:0.05-Dy^{3+},yEu^{3+}(y = 0–0.1)

Concentration	MYAS:xDy^{3+}	Concentration	MYAS:0.05Dy^{3+},yEu^{3+}
0.005	(0.3231, 0.3785)	0	(0.3485, 0.4068)
0.01	(0.3265, 0.3871)	0.005	(0.3530, 0.4053)
0.03	(0.3311, 0.3882)	0.01	(0.3562, 0.4047)
0.05	(0.3378, 0.3967)	0.03	(0.3777, 0.4037)
0.7	(0.3392, 0.3965)	0.05	(0.3882, 0.3971)
0.10	(0.3374, 0.3959)	0.07	(0.4071, 0.3944)
0.15	(0.3359, 0.3936)	0.10	(0.4258, 0.3890)

Fig. 16 shows the color coordinates of MYAS:0.05-Dy^{3+},yEu^{3+}(y = 0–0.1) and the warm white LEDs. The specific values are shown in Table 3. With an increase of Eu^{3+} concentration, the color coordinates of MYAS:0.05Dy^{3+},yEu^{3+} (y = 0–0.1) gradually transition from yellow to white and then to red. MYAS:0.05Dy^{3+},yEu^{3+} emitted white light with color coordinates of (0.4071, 0.3944) and color temperature of 3500 K. The warm white LED device was fabricated by combining the MYAS:0.05-Dy^{3+},0.07Eu^{3+} and a UV LED chip (370 nm) under a voltage of 3.2 V and current of 5 mA, and the CIE, CCT and CRI are (0.4071, 0.3944), 3500 K and 91.3, respectively.

4. Conclusions

A series of MYAS:xDy^{3+},yEu^{3+} phosphors were prepared by a high-temperature solid-state method. The fluorescent material of MYAS:xDy^{3+} can absorb UV light in the range of 250 nm to 400 nm. Under excitation of 367 nm UV light, MYAS:xDy^{3+} shows yellow emission, the optimal doping concentration is 0.05, and its concentration quenching mechanism involves dipole–dipole interaction. Through energy transfer, the luminous color of MYAS:xDy^{3+},yEu^{3+} can gradually change into warm white light with CIE chromaticity coordinates of (0.4071, 0.3944) and relative color temperature of 3500 K. A warm white LED device was fabricated by combining MYAS:0.05-Dy^{3+},0.07Eu^{3+} and a UV LED chip (370 nm), and the CIE, CCT and CRI are (0.4071, 0.3944), 3500 K and 91.3, respectively. Therefore, the MYAS:xDy^{3+},yEu^{3+} phosphors have potential application prospects in white LEDs.

Conflicts of interest

There are no conflicts to declare.

Acknowledgements

The work is supported by the Tangshan science and technology planning project (no. 19130201) and the National Natural Science Foundation of China (no. 51672066) and Foundation of Tangshan Normal University (2020A09).

References

1 S. Dutta, S. Som, M. M. Lal, *et al.* Multisite-Occupancy-Driven Intense Narrow-Band Blue Emission from $Sr_5SiO_4Cl_6$:Eu^{2+}

Phosphor with Excellent Stability and Color Pe, *Inorg. Chem.*, 2020, **59**(3), 1928–1939.

2 J. Meyer and F. Tappe, Solid-State Lighting: Photoluminescent Materials for Solid-State Lighting: State of the Art and Future Challenges, *Adv. Opt. Mater.*, 2015, **3**(4), 423.

3 C. H. Huang, T. M. Chen, W. R. Liu, *et al.* A single-phased emission-tunable phosphor $Ca_9Y(PO_4)_7$:Eu^{2+}, Mn^{2+} with efficient energy transfer for white-light-emitting diodes, *ACS Appl. Mater. Interfaces*, 2010, **2**(1), 259–264.

4 X. Y. Meng, K. L. Qiu, Z. Tian, *et al.* Tunable-emission single-phase phosphors $Ba_3Ca_2(PO_4)_3F$:M (M = Ce^{3+}, Eu^{2+}, Mn^{2+}): Crystal structure, luminescence and energy transfer, *J. Alloys Compd.*, 2017, **719**, 322–330.

5 Q. Liu, J. Guo, M. H. Fan, *et al.* Fast synthesis of Dy^{3+} and Tm^{3+} co-doped double perovskite $NaLaMgWO_6$: a thermally stable single-phase white-emitting phosphor for WLEDs, *J. Mater. Chem. C*, 2020, **8**, 2117–2122.

6 S. Petoud, S. M. Cohen, J. C. G. Bünzli, *et al.* Stable Lanthanide Luminescence Agents Highly Emissive in Aqueous Solution: Multidentate 2-Hydroxyisophthalamide Complexes of Sm^{3+}, Eu^{3+}, Tb^{3+}, Dy^{3+}, *J. Am. Chem. Soc.*, 2003, **125**, 13324–13325.

7 S. V. Eliseeva and C. G. Bünzli Jean, Lanthanide luminescence for functional materials and bio-sciences, *Chem. Soc. Rev.*, 2009, **39**(1), 189–227.

8 P. Han, P. J. Li, J. T. Zhang, *et al.* The effect of Li^+ ions on the luminescent properties of a single-phase white light-emitting phosphor α-$Sr_2P_2O_7$:Dy^{3+}, *Dalton Trans.*, 2015, **44**, 7854–7861.

9 G. Tiwari, N. Brahme, R. Sharma, *et al.* A study on the luminescence properties of gamma-ray-irradiated white light emitting $Ca_2Al_2SiO_7$:Dy^{3+} phosphors fabricated using a combustion-assisted method, *RSC Adv.*, 2016, **6**, 49317–49327.

10 P. Sehrawata, A. Khatkarb, S. Devia, *et al.* An effective emission of characteristic cool white light from Dy^{3+} doped perovskite type $SrLa_2Al_2O_7$ nanophosphors in single-phase pc WLEDs, *Chem. Phys. Lett.*, 2019, **737**, 136842–136871.

11 D. D. Xu, W. Zhou, Z. Zhang, S. J. Li, *et al.* Improved photoluminescence by charge compensation in Dy^{3+} doped $Sr_4Ca(PO_4)_2SiO_4$ phosphor, *Opt. Mater.*, 2019, **89**, 197–202.

12 Y. L. Zhang, M. H. Li, Z. H. Kong, *et al.* Plant habitat-conscious phosphors: Tuneable luminescence properties of Dy^{3+}-doped $Ca_8ZnY(PO_4)_7$ phosphors by co-dopants Mg^{2+} and B^{3+}, *Ceram. Int.*, 2020, **46**, 11717–11725.

13 S. Som, P. Mitra, V. Kumar, *et al.* The energy transfer phenomena and colour tunability in Y_2O_2S:Eu^{3+}/Dy^{3+} micro-fibers for white emission in solid state lighting applications, *Dalton Trans.*, 2014, **43**, 9860–9871.

14 C. H. Wang, Z. H. J. Wang, P. L. Li, *et al.* Relationships between luminescence properties and polyhedron distortion in $Ca_{9-x-y-z}Mg_xSr_yBa_zCe(PO_4)_7$:$Eu^{2+}$, Mn^{2+}, *J. Mater. Chem. C*, 2017, **5**, 10839–10846.

15 M. Xia, X. B. Wu, Y. Zhong, *et al.* Photoluminescence properties and energy transfer in a novel $Sr_8ZnY(PO_4)_7$:Tb^{3+}, Eu^{3+} phosphor with high thermal stability and its great potential for application in warm white light emitting diodes, *J. Mater. Chem. C*, 2019, **7**, 2927–2935.

16 C. H. Huang, W. R. Liu and T. M. Chen, Single-Phased White-Light Phosphors $Ca_9Gd(PO_4)_7$:Eu^{2+}, Mn^{2+} under Near-Ultraviolet Excitation, *J. Phys. Chem. C*, 2010, **114**(43), 18698–18701.

17 D. Q. Chen, S. Liu, Y. Zhou, *et al.* Dual-activator luminescence of RE/TM:$Y_3Al_5O_{12}$ (RE = Eu^{3+}, Tb^{3+}, Dy^{3+}; TM = Mn^{4+}, Cr^{3+}) phosphors for self-referencing optical thermometry, *J. Mater. Chem. C*, 2016, **4**, 9044–9051.

18 D. Huang, H. M. Zhu, Z. H. Deng, *et al.* Moisture-Resistant Mn^{4+}-Doped Core–Shell-Structured Fluoride Red Phosphor Exhibiting High Luminous Efficacy for Warm White Light-Emitting Diodes, *Angew. Chem., Int. Ed.*, 2019, **58**, 3843–3847.

19 L. Li, W. Zi, G. Li, *et al.* Hydrothermal synthesis and luminescent properties of $NaLa(MoO_4)_2$:Eu^{3+}, Tb^{3+} phosphors., *Cheminform*, 2013, **550**, 1–8.

20 Y. Liu, G. X. Liu, J. X. Wang, *et al.* Single-Component and Warm-White-Emitting Phosphor $NaGd(WO_4)_2$:Tm^{3+}, Dy^{3+}, Eu^{3+}: Synthesis, Luminescence, Energy Transfer, and Tunable Color, *Inorg. Chem.*, 2014, **53**, 11457–11466.

21 T. Q. Leow, H. Liu, R. Hussin, *et al.* Effects of Eu^{3+} and Dy^{3+} doping or co-doping on optical and structural properties of $BaB_2Si_2O_8$ phosphor for white LED applications, *J. Rare Earths*, 2016, **34**, 21–29.

22 S. k. K. Hussain, H. S. Go, J. J. Han, *et al.* Energy transfer mechanism and tunable emissions from $K_3La(VO_4)_2$:Dy^{3+}/Eu^{3+} phosphors and soft-PDMS-based composite films for multifunctional applications, *J. Alloys Compd.*, 2019, **805**, 1271–1281.

23 X. Min, X. W. Wu, Y. G. Liu, *et al.* Energy Transfer from Sm^{3+} to Eu^{3+} in Red-Emitting Phosphor $LaMgAl_{11}O_{19}$:Sm^{3+}, Eu^{3+} for Solar Cells and Near-Ultraviolet White Light-Emitting Diodes, *Inorg. Chem.*, 2014, **53**, 6060–6065.

24 X. Min, J. Xiao, M. H. Fang, Z. Huang, *et al.* Potassium-ion batteries: outlook on the present and future technologies, *Energy Environ. Sci.*, 2021, **14**, 2186–2243.

25 H. Tang, X. Y. Zhang, L. Cheng, J. Xie, *et al.* Broadband emission of $Lu_3Mg_2GaSi_2O_{12}$:Ce^{3+}, Sm^{3+} phosphors and their potential application for w-LEDs, *Ceram. Int.*, 2021, **35**, 1–11.

26 Z. F. Pan, Y. Xu, Q. S. Hu, *et al.* Combination cation substitution tuning of yellow-orange emitting phosphor $Mg_2Y_2Al_2Si_2O_{12}$:Ce^{3+}, *RSC Adv.*, 2015, **5**, 9489–9496.

27 Z. Wei, Y. Ji, M. Zhu, *et al.* Luminescence properties of garnet $Y_2Mg_2Al_2Si_2O_{12}$:Ce^{3+} phosphors, *Chem. Phys. Lett.*, 2021, **771**, 138516–138522.

28 X. Zhang, D. Zhang, D. Kan, *et al.* Crystal structure, luminescence properties and application performance of color tuning $Y_2Mg_2Al_2Si_2O_{12}$:Ce^{3+}, Mn^{2+} phosphors for warm white light-emitting diodes, *Mater. Adv.*, 2020, **1**, 2261–2270.

29 M. Yu, J. Lin, Z. Wang, *et al.* Fabrication, Patterning, and Optical Properties of Nanocrystalline YVO_4:A (A = Eu^{3+},

Dy^{3+}, Sm^{3+}, Er^{3+}) Phosphor Films *via* Sol–Gel Soft Lithography, *Chem. Mater.*, 2002, **14**(5), 2224–2231.

30 A. Kumar and J. Manam, Color tunable emission and temperature dependent photoluminescence properties of Eu^{3+} co-doped $Gd_2Zr_2O_7$:Dy^{3+} phosphors, *Opt. Mater.*, 2019, **96**, 109373–109383.

31 G. Annadural, S. M. M. KenneDy and V. Sivakumar, Synthesis of novel Dy^{3+} activated $Ba_2CaZn_2Si_6O_{17}$ phosphors for white light-emitting diodes, *Luminescence*, 2018, **33**, 521–527.

32 T. Nakajima and T. Tsuchiya, Plant Habitat-Conscious White Light Emission of Dy^{3+} in Whitlockite-like Phosphates: Reduced Photosynthesis and Inhibition of Bloom Impediment, *ACS Appl. Mater. Interfaces*, 2015, **7**, 21398–21407.

33 G. M. Rao, G. S. R. Raju, S. k. K. Hussain, *et al.* Tunable emissions *via* the white region from $Sr_2Gd_8(SiO_4)_6O_2$:RE^{3+} (RE^{3+}:Dy^{3+}, Tm^{3+}, Eu^{3+}) phosphors, *New J. Chem.*, 2016, **40**, 6214–6227.

34 M. Hermus, P. C. Phan, A. C. Duke, *et al.* Tunable optical properties and increased thermal quenching in the blue-emitting phosphor series: $Ba_2(Y_{1-x}Lu_x)_5B_5O_{17}$:$Ce^{3+}$ (x = 0–1), *Chem. Mater.*, 2017, **29**, 5267–5275.

35 Y. N. Zhou, W. D. Zhuang, Y. S. Hu, *et al.* Second-Sphere Polyhedron-Distortion-Induced Broadened and Red-Shifted Emission in $Lu_3(Mg_xAl_{2-x})(Al_{3-x}Si_x)O_{12}$:$Ce^{3+}$ for Warm WLED, *Inorg. Chem.*, 2019, **58**, 9108–9117.

36 Y. C. H. Lin, P. Erhart, M. Bettinelli, *et al.* Understanding the Interactions between Vibrational Modes and Excited State Relaxation in $Y_{3-x}Ce_xAl_5O_{12}$: Design Principles for Phosphors Based on 5d–4f Transitions, *Chem. Mater.*, 2018, **30**, 1865–1877.

37 S. H. X. Li, L. Wang, Q. Q. Zhu, *et al.* Crystal structure, tunable emission and applications of $Ca_{1-x}Al_{1-x}Si_{1+x}N_{3-x}O_x$:RE ($x$ = 0–0.22, RE = Ce^{3+}, Eu^{2+}) solid solution phosphors for white light-emitting diodes, *J. Mater. Chem. C*, 2016, **4**, 11219–11230.

38 X. Li, P. L. Li, Z. J. Wang, *et al.* Color-Tunable Luminescence Properties of Bi^{3+} in $Ca_5(BO_3)_3F$ *via* Changing Site Occupation and Energy Transfer, *Chem. Mater.*, 2017, **29**, 8792–8803.

39 C. H. Wang, Z. H. J. Wang, P. L. Li, *et al.* Relationships between luminescence properties and polyhedron distortion in $Ca_{9-x-y-z}Mg_xSr_yBa_zCe(PO_4)_7$:$Eu^{2+}$, Mn^{2+}, *J. Mater. Chem. C*, 2017, **5**, 10839–10846.

40 M. M. Tian, P. L. Li, Z. J. Wang, *et al.* Synthesis, color-tunable emission, thermal stability, luminescence and energy transfer of Sm^{3+} and Eu^{3+} single-doped $M_3Tb(BO_3)_3$ (M = Sr and Ba) phosphors, *CrystEngComm*, 2016, **18**, 6934–6947.